

**Magnetic dipole strength in  $^{128}\text{Xe}$  and  $^{134}\text{Xe}$  in the spin-flip resonance region**R. Massarczyk,<sup>1,2,\*</sup> G. Rusev,<sup>3</sup> R. Schwengner,<sup>1</sup> F. Dönau,<sup>1,†</sup> C. Bhatia,<sup>4</sup> M. E. Gooden,<sup>5,6</sup> J. H. Kelley,<sup>5,6</sup>  
A. P. Tonchev,<sup>7</sup> and W. Tornow<sup>5,8</sup><sup>1</sup>*Helmholtz-Zentrum Dresden-Rossendorf, 01328 Dresden, Germany*<sup>2</sup>*Technische Universität Dresden, 01062 Dresden, Germany*<sup>3</sup>*Los Alamos National Laboratory, Los Alamos, New Mexico 87545, USA*<sup>4</sup>*McMaster University, Hamilton, Ontario L8S4L8, Canada*<sup>5</sup>*Triangle Universities Nuclear Laboratory, Durham, North Carolina 27708, USA*<sup>6</sup>*North Carolina State University, Raleigh, North Carolina 27695, USA*<sup>7</sup>*Lawrence Livermore National Laboratory, Livermore, California 94550, USA*<sup>8</sup>*Duke University, Durham, North Carolina 27708, USA*

(Received 13 August 2014; revised manuscript received 25 September 2014; published 10 November 2014)

The magnetic dipole strength in the energy region of the spin-flip resonance is investigated in  $^{128}\text{Xe}$  and  $^{134}\text{Xe}$  using quasimonoeenergetic and linearly polarized  $\gamma$ -ray beams at the High-Intensity  $\gamma$ -Ray Source facility in Durham, North Carolina, USA. Absorption cross sections were deduced for the magnetic and electric dipole strength distributions separately for various intervals of excitation energy, including the strength of states in the unresolved quasicontinuum. The magnetic dipole strength distributions show structures resembling a resonance in the spin-flip region around an excitation energy of 8 MeV. The electric dipole strength distributions obtained from the present experiments are in agreement with the ones deduced from an earlier experiment using broad-band bremsstrahlung instead of a quasimonoeenergetic beam. The experimental magnetic and electric dipole strength distributions are compared with phenomenological approximations and with predictions of a quasiparticle random phase approximation in a deformed basis.

DOI: [10.1103/PhysRevC.90.054310](https://doi.org/10.1103/PhysRevC.90.054310)

PACS number(s): 25.20.-x, 21.60.-n, 24.30.Cz, 24.60.Ky

**I. INTRODUCTION**

Photon strength functions describing average electromagnetic transition strengths are a critical input to statistical reaction codes such as TALYS [1] that are used to calculate cross sections of photonuclear reactions and of the inverse radiative capture reactions. Radiative neutron capture is one of the basic processes for the synthesis of heavy elements in stellar environments and relevant for next-generation nuclear technologies. It has been shown that the dipole strength distribution in the energy region below the neutron separation energy has a direct influence on neutron capture rates [2,3]. Modifications of the dipole strength at low excitation energies considerably change the calculated relative abundances of several isotopes in the solar system [4]. Therefore, precise strength functions are important for an improved description of neutron capture and, consequently, for a higher accuracy of network calculations describing the synthesis of heavy elements.

The electric dipole ( $E1$ ) strength is dominated by the isovector giant dipole resonance (GDR), which may be approximated by a Lorentz function [5,6]. Combinations of two or three Lorentz functions are used to describe the double or triple humps of the GDR in nuclei with quadrupole or triaxial deformation [7–9]. Our recent study of  $E1$  strength functions in the chain of xenon isotopes revealed that the enhanced strength observed on the low-energy tail of the GDR correlates with neutron excess rather than with nuclear deformation [10].

The magnetic dipole ( $M1$ ) strength is believed to contain contributions of two types of excitation. First, the scissors mode appears in deformed nuclei at around 3 MeV and is interpreted as a vibration of the deformed proton and neutron systems against each other [11–13]. It was found that the summed magnetic dipole strength  $\sum B(M1)$  in the energy region of the scissors mode is proportional to the square of the quadrupole deformation  $\beta_2$  [12,14]. In addition to excitations from the ground state, this mode was observed also for de-excitations of higher-lying states [15]. Second, the spin-flip mode typically appears around 8 MeV [13]. This mode is considered to split into isoscalar and isovector parts [16]. Their centroid energies can be described by  $B_{\text{is}} = 34 A^{-1/3}$  MeV and  $B_{\text{iv}} = 44 A^{-1/3}$  MeV, respectively [17]. The spin-flip mode is assumed to be uncorrelated with nuclear deformation.

In addition to these modes, experiments on  $^{56,57}\text{Fe}$  [18],  $^{60}\text{Ni}$  [19], Mo isotopes [20], and  $^{105,106}\text{Cd}$  [21] found an enhancement of dipole strength functions toward very low  $\gamma$ -ray energy, which can be explained by high  $B(M1)$  strengths between close-lying states with specific configurations including valence protons and neutrons in high- $j$  orbits [22]. An alternative explanation is an enhanced electric dipole strength as proposed in Ref. [23].

**II. EXPERIMENTAL FACILITY AND METHODS**

In this work we describe experiments using photon scattering, also called nuclear resonance fluorescence, on the two isotopes  $^{128}\text{Xe}$  and  $^{134}\text{Xe}$ . The experiments were carried out at the High-Intensity  $\gamma$ -Ray Source (HI $\gamma$ S) [24] operated by the Triangle Universities Nuclear Laboratory (TUNL) in Durham, North Carolina. The highly polarized  $\gamma$ -ray

\*Present address: Los Alamos National Laboratory, Los Alamos, New Mexico 87545, USA; r.massarczyk@hzdr.de

†Deceased.

beams of the HI $\gamma$ S allowed us to distinguish unambiguously between  $E1$  and  $M1$  radiations and, hence, to investigate the structure of the  $M1$  strength distribution. We focus on the unexplored energy range of the spin-flip mode. Excitations in the range of the scissors mode were studied earlier at the Stuttgart Dynamitron [25] and a relation between quadrupole deformation and the strength and position of the scissors mode was derived. In recent nuclear resonance fluorescence experiments at the bremsstrahlung facility  $\gamma$ ELBE [26] we deduced photoabsorption cross sections of various Xe isotopes and studied their evolution with nuclear deformation and neutron excess [10]. Using the polarization information from measurements at HI $\gamma$ S, one finds that the photoabsorption cross sections are dominated by the  $E1$  part, whereas the structure of  $M1$  contributions was not studied in that work.

$\gamma$ -ray beams at the HI $\gamma$ S are produced by Compton backscattering of a high-intensity free-electron laser (FEL) beam from relativistic electrons circulating in the Duke storage ring. Presently, the energy of the backward scattered photons can be tuned over a wide energy range, from 1 to about 100 MeV, by changing the energy of the electron beam and the FEL wavelength [24]. The polarization of the FEL photons, defined by the magnetic field of the undulators, is mostly preserved during the Compton backscattering due to a negligible recoil effect, leading to the production of intense photon beams with a degree of polarization of nearly 100%. In addition, the beams are quasimonoenergetic, with an energy spread of about 3% using a 30.5-cm-long lead collimator with a cylindrical hole of 1.9-cm diameter positioned 56 m downstream from the collision point of the electrons with the FEL photons. Photon-beam energies of  $E_\gamma = 6.0$ –9.6 MeV in 300-keV steps were chosen, allowing us to investigate excitations up to the neutron separation energies of 9.6 MeV ( $^{128}\text{Xe}$ ) and 8.5 MeV ( $^{134}\text{Xe}$ ) without any gaps in between. A high-purity germanium (HPGe) detector, placed a short distance behind the target position, was used to measure the energy distribution of the impinging beam. An example of a measured energy distribution is shown in Fig. 1. The spectra were unfolded for detector response and for the effect of copper flux attenuators that were placed in the beam to avoid pileup and long dead times. The response functions of the detectors were deduced after combination of multiple source measurements and simulations using the GEANT4 package [27]. The measured distributions are in agreement with the predictions given in Refs. [28] and [29], which are also shown in Fig. 1.

The targets used were high-pressure gas targets as described in Ref. [30]. Spherical containers made of stainless steel with an inner diameter of 20 mm and a wall thickness of 0.6 mm were filled with xenon gas enriched to over 99% in  $^{128}\text{Xe}$  or  $^{134}\text{Xe}$ , respectively. The masses were 0.92 g of  $^{128}\text{Xe}$  and 1.52 g of  $^{134}\text{Xe}$ . Scattered photons were measured with HPGe detectors placed perpendicular to the beam axis at azimuthal angles of  $0^\circ$ ,  $90^\circ$ ,  $180^\circ$ , and  $270^\circ$ ; i.e., two were placed parallel and two perpendicular to the polarization plane, allowing the distinction between electric and magnetic character of the scattered radiation [31,32]. In addition, a fifth detector was placed under a backward polar angle ( $125^\circ$ ) in the

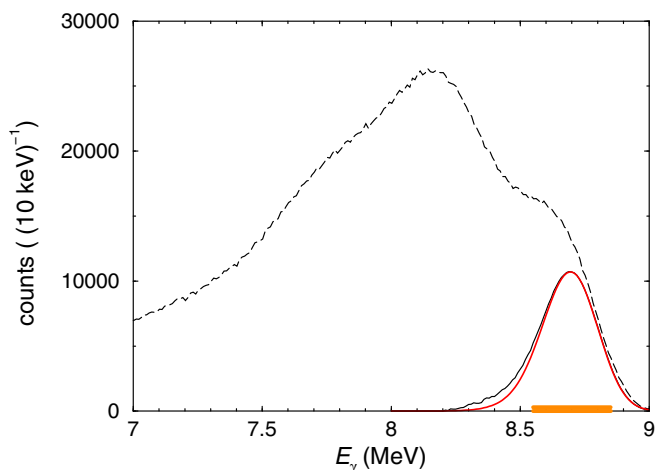


FIG. 1. (Color online) Spectrum of incident photon energies for the beam setting for  $E_\gamma = 8.7$  MeV. The solid black curve shows the beam distributions corrected for detector response and attenuator effects, while the dashed curve is the uncorrected spectrum. The lower solid (red) curve is the calculated beam distribution in relativistic Compton backscattering following Ref. [28]. The horizontal (orange) bar indicates the region of analysis for these beam parameters.

plane perpendicular to the polarization axis. Magnetic dipole transitions occur under all angles within this plane, whereas electric quadrupole transitions dominate under  $90^\circ$  due to their angular distribution.

Typical spectra are shown in Fig. 2 for a beam energy of 7.5 MeV. These spectra contain peaks of the individual

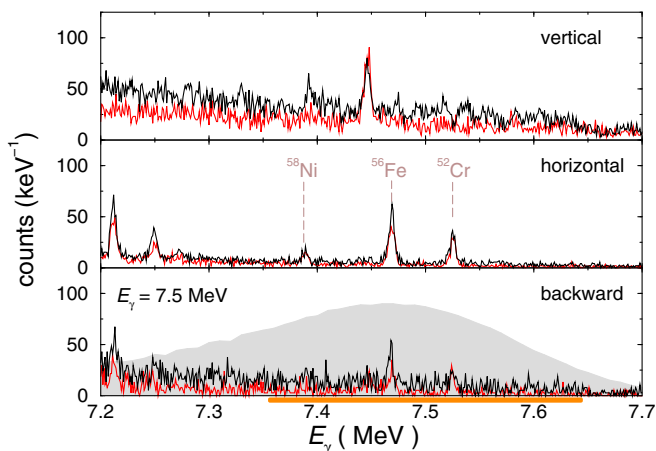


FIG. 2. (Color online) Spectra measured using  $E_\gamma = 7.5$  MeV photons for the two Xe isotopes [lighter (red) lines and black lines, respectively]. Prominent  $M1$  transitions from the steel container are labeled with the corresponding isotopes. The horizontal (orange) bar indicates the analysis region chosen for this beam energy. The shaded (gray) area in the bottom panel shows the incident beam profile as described in the text. Vertical detectors are sensitive to  $E1$  transitions. The combination of horizontal and backward detector allows identification of the  $M1$  strength. Spectra measured in the backward and horizontal detectors are corrected for their efficiency relative to the pair of vertical detectors.

Xe isotopes and peaks appearing for both targets. These are transitions of nuclides contained in the steel sphere.  $\gamma$  rays emitted from the steel components are well known and belong mainly to the isotopes  $^{52}\text{Cr}$ ,  $^{54,56}\text{Fe}$ , and  $^{58,60}\text{Ni}$ . The contribution of the respective xenon isotope to the spectrum was deduced by subtracting the steel peaks from the spectrum in the analyzed energy region of 300-keV width. As the spectra of the light steel components contain comparably few isolated peaks, there is only a small contribution to the detector response. In the narrow analysis interval of 300 keV for each beam energy the detector response has a small effect only because the main part of the Compton continuum as well as single- and double-escape peaks appear at photon energies below  $E_\gamma - 300$  keV. The correction for detector response was applied to the full intensity of the analyzed section of the spectrum including resolved peaks and the quasicontinuum of unresolved states in the respective Xe isotope. The intensity of the background caused by atomic processes in target material and steel drops toward a high energy and is negligible in the excited energy region as shown for earlier measurements using the same setup [33].

We calculated the photoabsorption cross sections relative to known ones in Fe isotopes. Alternatively, cross sections in the Xe isotopes determined in our previous experiments with bremsstrahlung [10] could have been used. We will show that the two independent ways lead to compatible results. We used the following relation for the calculation of the photoabsorption cross section relative to the known quantities of transitions in Fe isotopes:

$$\frac{A_{\text{Fe}}(E)}{A_{\text{Xe}}(E)} = \frac{I_{\text{Fe}}\left(\frac{\Gamma_{0,\text{Fe}}}{\Gamma_{\text{Fe}}}\right)\varepsilon_{\text{Fe}} \int N_{\text{Fe}}(\vec{r})\Phi_{\text{Fe}}(E,\vec{r})d\vec{r}}{I_{\text{Xe}}\left(\frac{\Gamma_{0,\text{Xe}}}{\Gamma_{\text{Xe}}}\right)\varepsilon_{\text{Xe}} \int N_{\text{Xe}}(\vec{r})\Phi_{\text{Xe}}(E,\vec{r})d\vec{r}}. \quad (1)$$

Here,  $A_{\text{Fe}}$  and  $A_{\text{Xe}}$  are the counts in a peak of a known transition in  $^{56}\text{Fe}$  and the total number of counts in the region of analysis for a xenon isotope, respectively. Peaks of nuclides in the steel container appear in the spectra measured with each of the two xenon isotopes and can therefore be clearly identified. For each detector pair (detecting  $M1$  or  $E1$  transitions) the intensity in the spectrum after subtracting the peaks belonging to the steel components was analyzed. Contributions from the nuclei in the steel container to the quasicontinuum have been neglected, because the level densities of these light nuclei are comparably small at the studied excitation energies. The reference peak in  $^{56}\text{Fe}$  may appear in the vertical or in the horizontal detectors. We found transitions in  $^{56}\text{Fe}$  that could be used as a reference in all energy intervals except for one. In this interval around 6 MeV a transition in  $^{58}\text{Fe}$  was used. To obtain the correct number  $A_{\text{Xe}}$ , the events were weighted with the incoming normalized flux distribution shown in Fig. 1.

$I_{\text{Fe}}$  is the energy-integrated absorption cross section of a state in  $^{56}\text{Fe}$ . It is connected with the scattering cross section for the ground state  $I_0$  given in Refs. [34] and [35] via the relation  $I_0 = I_{\text{Fe}}\left(\frac{\Gamma_{0,\text{Fe}}}{\Gamma_{\text{Fe}}}\right)$ , with  $\Gamma_0$  and  $\Gamma$  being the partial width of the ground-state transition and the level width, respectively. For the xenon isotopes the integrated absorption cross section was deduced as  $I_{\text{Xe}} \approx \sigma_\gamma(E_x)\Delta E$ , with  $\Delta E = 0.3$  MeV being the region of analysis.

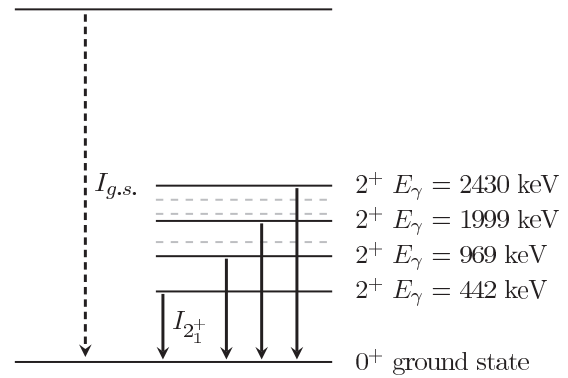


FIG. 3. Transitions in  $^{128}\text{Xe}$  used to estimate the branching ratios of inelastic transitions. The dashed arrow stands for the bunch of ground-state transitions. Solid arrows mark transitions depopulating known low-lying states assumed to collect most of the inelastic transitions from higher-lying levels. Dashed gray lines indicate known states not decaying directly to the ground state and therefore not considered in the analysis.

The quantity  $\varepsilon_{\text{Fe}}/\varepsilon_{\text{Xe}}$  is the ratio of the efficiencies of the pairs of vertical and horizontal detectors in which the respective Fe peaks and Xe energy regions were analyzed.  $N_{\text{Fe}}(\vec{r})$ ,  $N_{\text{Xe}}(\vec{r})$  are the mass distribution of Fe and Xe nuclei, respectively, in the beam. The two factors  $\Phi_{\text{Fe}}(E,\vec{r})$  and  $\Phi_{\text{Xe}}(E,\vec{r})$  take into account that the energy distribution is not flat over the beam profile. According to Refs. [28] and [29] the beam profile changes with the distance from the beam axis. Because the mass distributions of the xenon gas and the surrounding steel sphere do not have the same gradient, an extra correction was applied taking into account the crossover of areal mass and energy trends.

The ratio  $\Gamma_{0,\text{Xe}}/\Gamma_{\text{Xe}}$  is the average branching ratio  $b_0$  of ground-state transitions for the xenon isotopes in a given energy interval. This value takes into account that excited states do not necessarily de-excite directly to the ground state. In analogy to previous work [38–40], the branching ratios were deduced as the ratios of the intensities of the ground-state transitions and the intensities of transitions depopulating low-lying states as illustrated in Fig. 3 for the case of  $^{128}\text{Xe}$ :

$$b_0 = \frac{I_0}{I_0 + I_{2_1^+} + I_{2_2^+} + \dots}. \quad (2)$$

Here,  $I_0$  and  $I_{2_1^+}$  stand for the efficiency-corrected intensities of the transitions from a state in the excited energy region to the ground state and from the first excited state to the ground state, respectively. The transitions from the lowest excited states are assumed to collect the main part of the intensities of inelastic transitions from the high-lying excited states. This means that transitions bypassing these states are neglected. The intensities of the ground-state transitions from high-lying states were corrected for the angular distribution taking into account the de-excitation after an excitation of a spin-1 state with polarized photons [39]. For the intensities of the  $2^+ \rightarrow 0_1^+$  transitions the angular distributions are assumed to be unity because these

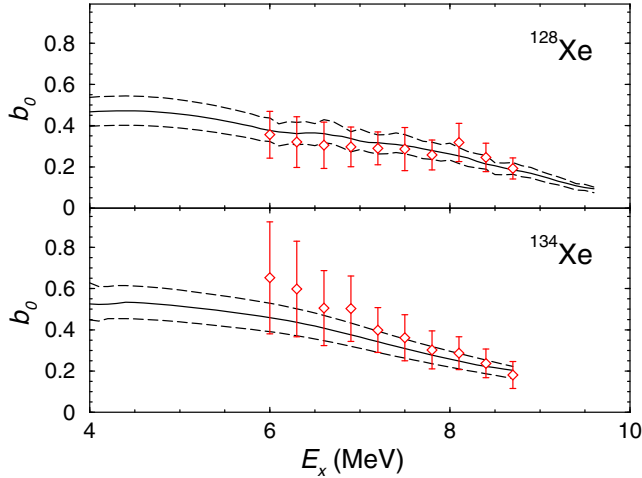


FIG. 4. (Color online) Branching ratios deduced from the present experiments [(red) diamonds] and results of  $\gamma$ -ray cascade simulations using the code  $\gamma$ DEX (solid black curves) and their uncertainty bands (dashed black curves).

states are fed by several cascade transitions washing out the angular correlations.

For  $^{128}\text{Xe}$  the transitions depopulating the known lowest four states to the ground state [41] were considered as illustrated in Fig. 3. In  $^{134}\text{Xe}$ , only the first two excited  $2^+$  states are known [41] and were taken into account. A further complication is that the energy of the first excited state in  $^{134}\text{Xe}$  coincides with the one in  $^{56}\text{Fe}$  at 847 keV. The intensity of the transition in  $^{56}\text{Fe}$  was estimated from the ratio to the intensity of the transition from the second excited state in  $^{56}\text{Fe}$  determined from the spectrum measured with  $^{128}\text{Xe}$  and was subtracted from the peak observed in the spectrum of  $^{134}\text{Xe}$ . This was possible because the two steel containers are nearly identical. The average branching ratios determined in this way for the energy regions excited in the present experiments are shown in Fig. 4.

The present experimental branching ratios can be used to test branching ratios determined from our earlier experiments using bremsstrahlung at  $\gamma$ ELBE. In the analysis of the data from those experiments, branching ratios were calculated in connection with simulations of statistical  $\gamma$ -ray cascades using the code  $\gamma$ DEX [36,37]. The present experimental values are compared with the results of  $\gamma$ DEX in Fig. 4. The uncertainties of the simulated branching ratios arise from a random variation of the level density parameters within their uncertainties. As shown in the upper panel, the  $\gamma$ DEX results agree well with the experimental values. This proves the reliability of the input parameters for the statistical model underlying the cascade simulations. The larger uncertainties found in the experimental data of  $^{134}\text{Xe}$  shown in the lower panel are caused by the subtraction of the iron peak from the peak of the first  $2^+$  state in  $^{134}\text{Xe}$ . Taking into account the information about the lowest two excited  $2^+$  states only, the branching ratios tend to be too large. The inclusion of additional intensities  $I_{2,3,4,\dots}^+$  may scale down the ratios in Eq. (2).

The model-independent branching ratios deduced from the present experiments at the HI $\gamma$ S have been used for the

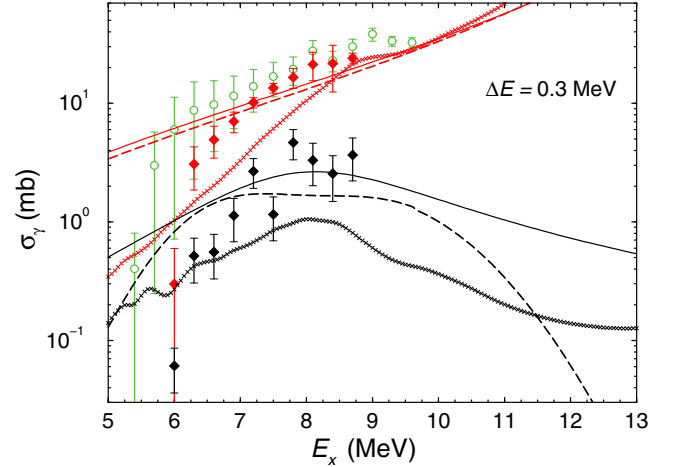


FIG. 5. (Color online) Photoabsorption cross sections for  $^{128}\text{Xe}$  deduced from the present experiments at HI $\gamma$ S for the  $E1$  part [(red) diamonds] and the  $M1$  part (black diamonds). For comparison, data from our earlier experiment at  $\gamma$ ELBE [10] including both  $E1$  and  $M1$  contributions [open (green) circles], in 0.3-MeV energy bins, are shown. In addition, predictions of phenomenological expressions are given. RIPL3 [6] recommendations for the  $E1$  and  $M1$  parts are plotted as lighter (red) and black solid curves, respectively. The TLO model [9] for  $E1$  and the triple-Gaussian model [36] for  $M1$  are shown as lighter (red) and black dashed curves, respectively. Lighter (red) and black Xs represent the result of QRPA calculations for the  $E1$  and  $M1$  strength, respectively.

calculation of the photoabsorption cross sections. For the reference cross sections in iron the branching ratios have to be taken as unity, as they are included in the values of the cross sections given in the literature.

### III. RESULTS

Photoabsorption cross sections were calculated using Eq. (1). For each detector pair an  $E1$  and an  $M1$  component was deduced. The main contribution of 20% to their uncertainties emerges from the normalization of xenon values to cross sections in iron, which involves the uncertainty of the number of atoms in the steel container covered by the beam spot. The results for  $^{128}\text{Xe}$  and  $^{134}\text{Xe}$  are shown in Figs. 5 and 6, respectively. The  $E1$  parts are compared with the results of our previous measurements using bremsstrahlung at  $\gamma$ ELBE [10]. The good agreement of the data from  $\gamma$ ELBE and HI $\gamma$ S within the uncertainties for the two isotopes in the energy range from about 6.6 to 8.7 MeV proves the accuracy of the normalization to the cross sections of the peaks of the Fe isotopes just described. Below 6.6 MeV, the uncertainties of the  $\gamma$ ELBE data become large and the cross sections may be slightly overestimated. One reason for the larger deviation in  $^{134}\text{Xe}$  compared with  $^{128}\text{Xe}$  may be the difference in the calculated and experimentally deduced branching ratios. As one can see in Fig. 4, the branching ratios calculated with  $\gamma$ DEX and used in Ref. [37] underestimate the experimental branching ratios deduced in this work. A higher number of bypassing transitions would result in a lower branching ratio and, therefore, in a greater cross section. Data for  $^{128}\text{Xe}$  at



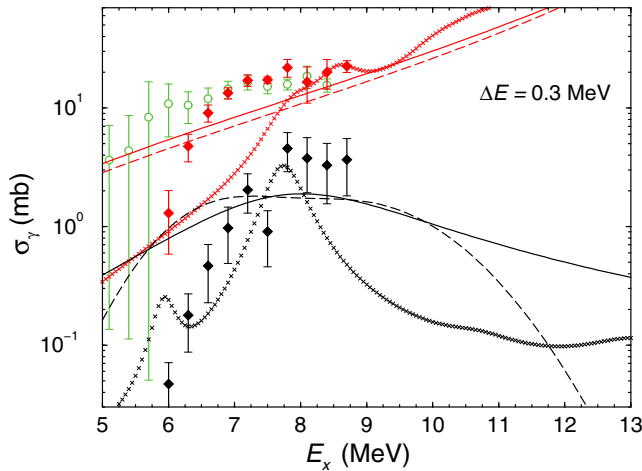


FIG. 6. (Color online) Photoabsorption cross sections for  $^{134}\text{Xe}$ . For the definition of the symbols and curves see the caption to Fig. 5.

higher energies are not included because normalization to peaks of the steel container is difficult above 9 MeV. For  $^{134}\text{Xe}$  a significant number of scattered events above the threshold was found at the highest excitation energy.

For comparison, predictions of phenomenological parametrizations for the  $E1$  cross sections as given in the RIPL3 database [6] and of the triple-Lorentzian (TLO) model [9] are shown. The  $E1$  strength on the low-energy tail of the GDR is underestimated by the RIPL3 and TLO predictions. This trend was also found for the isotopes  $^{124}\text{Xe}$ ,  $^{130}\text{Xe}$ , and  $^{132}\text{Xe}$  studied at  $\gamma\text{ELBE}$  [10].

The  $M1$  cross sections show distributions around 8 MeV that resemble the low-energy part of a resonance, where the continuation toward energies beyond 9 MeV remains unexplored. The parametrization of the magnetic dipole strength in RIPL3 [6] proposes a Lorentz function scaled to the  $E1$  strength at 7 MeV. The ratio between the two strength functions is given as

$$\frac{f_{E1}(7\text{MeV})}{f_{M1}(7\text{MeV})} = \frac{\sigma_{\gamma,E1}(7\text{MeV})}{\sigma_{\gamma,M1}(7\text{MeV})} = 0.0588A^{0.878}. \quad (3)$$

The transformation from strength function to cross section followed the procedure given in Ref. [42]. The ratios obtained from Eq. (3) are 4.1 for  $^{128}\text{Xe}$  and 4.3 for  $^{134}\text{Xe}$ , whereas the ratios obtained from the present experimental cross sections are 4.9(18) and 10.7(56), respectively. The uncertainties are mainly caused by the low counting statistics and the uncertainty in the mass of the reference isotope. The second parametrization of the  $M1$  strength shown in Figs. 5 and 6 is the triple-Gaussian parametrization given in Ref. [36]. This distribution and total amount of  $M1$  strength are based on those presented in Ref. [13]. This approach has the advantage that it predicts an  $M1$  strength function independent of the  $E1$  strength function and takes into account the splitting into scissors mode, isoscalar and isovector spin-flip excitations. The centroid of the strength seems to be predicted well by both approximations, but none of these descriptions can predict the shape and order of magnitude of the experimental cross section satisfactorily. In comparison to the triple-Gaussian

model one may suspect that the experimental data show the isoscalar spin-flip mode, whereas the isovector spin-flip mode appears at higher energies. The broad distributions of the Lorentz functions according to the RIPL3 recommendation overestimate the tail of the experimental distribution at least toward low energies.

In addition to the phenomenological models, we have calculated cross sections of  $E1$  and  $M1$  excitations within a quasiparticle random phase approximation (QRPA) in a deformed Woods-Saxon basis, which is described in detail in Refs. [43–45]. The deformation parameters used as input were taken from Ref. [46] and are identical to those used in Ref. [10]. The QRPA solutions were smeared with Lorentzian functions of an energy-dependent width  $\Gamma(E) = 2.5(E/15)^2$  MeV. As one can see in Figs. 5 and 6, the QRPA results for the  $E1$  part underestimate the experimental data toward low energies as found in our earlier studies [10,33]. The calculated  $M1$  strength distributions reproduce qualitatively the experimental structures and describe the widths of the experimental resonances much better than the phenomenological approximations do. However, the magnitude of the calculated cross section in  $^{128}\text{Xe}$  is a factor of about 3 too small compared with the experimental values.

#### IV. SUMMARY

Summarizing, we have deduced the  $E1$  and  $M1$  contributions to the photoabsorption cross section in  $^{128}\text{Xe}$  and  $^{134}\text{Xe}$  in an experiment using the polarized and quasimonochromatic  $\gamma$ -ray beams at the HI $\gamma$ S facility. In the analysis, the photon flux was calibrated using known level widths of components of the steel container. The results of this analysis are consistent with results of an earlier experiment using bremsstrahlung, which proves the reliability of the calibration. Intensities of inelastic transitions were determined from the intensities of transitions from known low-lying states, and intensities in the continuum parts of the xenon spectra were taken into account as well.

The magnetic dipole parts of the absorption cross section obtained in the present work display structures resembling the low-energy parts of resonances around 8 MeV. They may represent the spin-flip modes expected in this energy region. These cross sections provide novel experimental information about  $M1$  strength distributions, which is scarce for the energy region considered. Phenomenological approximations of the  $M1$  strength give distributions that are too broad compared to our experimental results. Microscopic QRPA calculations describe the shape of the experimental  $M1$  resonances relatively well but predict a strength that is too low in the case of  $^{128}\text{Xe}$ . The continuation of the strength toward a higher energy beyond the neutron separation threshold remains an open question.

Altogether, the  $M1$  strength contributes about 10% to the total absorption cross section. However, as demonstrated in Refs. [2] and [4], even a little additional strength on top of the tail of the GDR can have significant consequences for neutron capture reaction rates. Therefore, the precise investigation of  $M1$  strength functions is important to improve the input to statistical reaction codes and network calculations.

In addition, the branching ratios and cross sections deduced from the present experiments were used to test the results of our earlier experiment with bremsstrahlung at  $\gamma$ ELBE. In the analysis of that experiment, branching ratios were determined from simulations of statistical  $\gamma$ -ray cascades using the code  $\gamma$ DEX. The good agreement of the model-independent results of the present experiments at the HI $\gamma$ S with those obtained from  $\gamma$ ELBE data proves the reliability of the statistical model parameters used in the analysis of the  $\gamma$ ELBE data.

## ACKNOWLEDGMENTS

We thank A. Hartmann for the target preparation and the crew of the HI $\gamma$ S facility for their collaboration during the experiments. This work was supported by the German Research Foundation (DFG), Project No. SCHW883/1-1 and EURATOM FP7 Project ERINDA (FP7-269499). Partial support was also given by the U.S. Department of Energy, Office of Nuclear Physics, under Grants No. DE-FG02-97ER41033 and No. DE-FG02-97ER41042.

- 
- [1] <http://www.talys.eu/>.
- [2] M. Beard, S. Frauendorf, B. Kämpfer, R. Schwengner, and M. Wiescher, *Phys. Rev. C* **85**, 065808 (2012).
- [3] H. P. Loens *et al.*, *Eur. Phys. J. A* **48**, 34 (2012).
- [4] S. Goriely, *Phys. Lett. B* **436**, 10 (1998).
- [5] P. Axel, *Phys. Rev.* **126**, 671 (1962).
- [6] R. Capote *et al.*, *Nucl. Data Sheets* **110**, 3107 (2009).
- [7] A. Bohr and B. R. Mottelson, *Nuclear Structure, Vol. II*, (W. A. Benjamin, Reading, MA, 1975).
- [8] J. M. Eisenberg and W. Greiner, *Nuclear Theory, Vol. I*, (North-Holland, Amsterdam, 1975).
- [9] A. R. Junghans, G. Rusev, R. Schwengner, A. Wagner, and E. Grosse, *Phys. Lett. B* **670**, 200 (2008).
- [10] R. Massarczyk *et al.*, *Phys. Rev. Lett.* **112**, 072501 (2014).
- [11] A. Richter, *Nucl. Phys. A* **507**, 99 (1990).
- [12] W. Ziegler *et al.*, *Phys. Rev. Lett.* **65**, 2515 (1990).
- [13] K. Heyde, P. von Neumann-Cosel, and A. Richter, *Rev. Mod. Phys.* **82**, 2365 (2010).
- [14] J. Margraf *et al.*, *Phys. Rev. C* **47**, 1474 (1993).
- [15] M. Guttormsen *et al.*, *Phys. Rev. Lett.* **109**, 162503 (2012).
- [16] D. Frekers *et al.*, *Phys. Lett. B* **244**, 178 (1990).
- [17] A. Richter, *Prog. Part. Nucl. Phys.* **34**, 261 (1995).
- [18] A. Voinov *et al.*, *Phys. Rev. Lett.* **93**, 142504 (2004).
- [19] A. Voinov *et al.*, *Phys. Rev. C* **81**, 024319 (2010).
- [20] M. Guttormsen *et al.*, *Phys. Rev. C* **71**, 044307 (2005).
- [21] A. C. Larsen *et al.*, *Phys. Rev. C* **87**, 014319 (2013).
- [22] R. Schwengner, S. Frauendorf, and A. C. Larsen, *Phys. Rev. Lett.* **111**, 232504 (2013).
- [23] E. Litvinova and E. Below, *Phys. Rev. C* **88**, 031302(R) (2013).
- [24] H. R. Weller *et al.*, *Prog. Part. Nucl. Phys.* **62**, 257 (2009).
- [25] H. von Garrel *et al.*, *Phys. Rev. C* **73**, 054315 (2006).
- [26] R. Schwengner *et al.*, *Nucl. Instrum. Methods Phys. Res. A* **555**, 211 (2005).
- [27] S. Agostinelli *et al.*, *Nucl. Instrum. Meth. A* **506**, 250 (2003).
- [28] C. Sun *et al.*, *Phys. Rev. ST Accel. Beams* **12**, 062801 (2009).
- [29] C. Sun *et al.*, *Phys. Rev. ST Accel. Beams* **14**, 044701 (2011).
- [30] G. Rupp *et al.*, *Nucl. Instrum. Meth. A* **608**, 152 (2009).
- [31] N. Pietralla *et al.*, *Phys. Rev. C* **65**, 047305 (2002).
- [32] A. Tonchev *et al.*, *Phys. Rev. Lett.* **104**, 072501 (2010).
- [33] R. Massarczyk *et al.*, *Phys. Rev. C* **86**, 014319 (2012).
- [34] T. Chapuran *et al.*, *Phys. Rev. C* **30**, 54 (1984).
- [35] F. Bauwens *et al.*, *Phys. Rev. C* **62**, 024302 (2000).
- [36] G. Schramm *et al.*, *Phys. Rev. C* **85**, 014311 (2012).
- [37] R. Massarczyk *et al.*, *Phys. Rev. C* **87**, 044306 (2013).
- [38] G. Rusev *et al.*, *Phys. Rev. Lett.* **110**, 022503 (2013).
- [39] P. M. Goddard *et al.*, *Phys. Rev. C* **88**, 064308 (2013).
- [40] G. Rusev *et al.*, *AIP Conf. Proc.* **1099**, 799 (2009).
- [41] <http://www.nndc.bnl.gov/ensdf/>.
- [42] G. A. Bartholomew, E. D. Earle, A. J. Ferguson, J. W. Knowles, and M. A. Lone, in *Advances in Nuclear Physics*, edited by M. Baranger and E. Vogt, Vol. 7 (Springer, Berlin, 1973), pp. 229-324.
- [43] F. Dönau, *Phys. Rev. Lett.* **94**, 092503 (2005).
- [44] S. Q. Zhang, I. Bentley, S. Brant, F. Dönau, S. Frauendorf, B. Kämpfer, R. Schwengner, and A. Wagner, *Phys. Rev. C* **80**, 021307 (2009).
- [45] I. Bentley, S. Brant, F. Dönau, S. Frauendorf, B. Kämpfer, R. Schwengner, and S. Q. Zhang, *Phys. Rev. C* **83**, 014317 (2011).
- [46] P. Möller *et al.*, *Atom. Data Nucl. Data Tables* **59**, 185 (1995).